Broadband Cross-Slotted Patch Antenna for 5G Millimeter-Wave Applications Based on Characteristic Mode Analysis

Jiangcheng Chen, *Graduate Student Member, IEEE*, Markus Berg, Kimmo Rasilainen, *Member, IEEE*, Zeeshan Siddiqui, *Graduate Student Member, IEEE*, Marko E. Leinonen, *Member, IEEE*, and Aarno Pärssinen, *Senior Member, IEEE*

***Abstract*— This article proposes a wideband differentially fed dual-polarized magnetoelectric (ME) dipole for millimeter-wave (mm-Wave) applications. Various electric and magnetic characteristic modes of a slotted patch antenna are investigated and utilized effectively to create a stable broadside radiation pattern, covering fifth-generation (5G) frequency bands from 24.25 to 40 GHz. To implement this, the lifted ground (LGND) concept is applied to achieve a 57.1% impedance bandwidth for a single antenna element. In addition, the three resonances of the antenna can be manipulated independently. The use of differential feeding allows more than 36 dB of port-to-port isolation across the entire operating band. The measured gains of the single element and 2 × 2 array are 8.4 and 13.4 dBi, respectively. Also, the measured results indicate symmetrical E- and H-plane radiation patterns and cross-polarization levels lower than −26 dB. With the favorable electrical performance, compact size, simple structure, and low-cost fabrication, the proposed ME dipole is a promising candidate for mm-Wave Antenna-in-Package (AiP) applications.**

***Index Terms*— Characteristic mode analysis (CMA), complementary antenna, dual-polarized antenna, fifth generation (5G), magnetoelectric (ME) dipole, millimeter-wave (mm-Wave), ring patch antenna.**

I. Introduction

THE WIRELESS industry is shifting toward its fifth generation (5G) of cellular technology that will employ millimeter-wave (mm-Wave) frequencies to offer unprecedented spectrum and multi-gigabit-per-second (Gbps) data rates to mobile devices [1], [2]. In recent years, a portion of the mm-Wave spectrum consisting of the 24/28/38/39 GHz subbands at the Ka-band, referred to as 5G New Radio FR2 bands, has been allocated for upcoming 5G mobile communications [3]. In addition to a wide operation range, link budget analysis shows stringent requirements for array gain and the performance of individual antenna elements [4]. To integrate multiple subfrequency bands into a single antenna element, a broadband antenna element covering all desired subbands with a simple feeding configuration for the sake of miniaturization and ease of integration with Antenna-in-Package (AiP) technology is preferred [5]. Furthermore, dual-polarized operation with high cross-polarization discrimination (XPD) is also a necessity due to the increased channel capacity and reduced side effects of multipath fading provided by polarization diversity [6], [7].

Various antenna designs have been proposed to obtain the required characteristics. Among these reported antennas, traditional microstrip patch antennas [8], [9] with single resonance can support the 28 GHz band only, which is not desired. Instead, one of the possible solutions is to cover the subbands of the 5G lower band (LB) ranging from 24.25 to 29.5 GHz (19.53%) and upper band (UB) from 37 to 40 GHz (7.79%). Substrate-integrated waveguide (SIW) antennas [10], [11], [12] have been proposed for dual-band operation with compact dimensions caused by the quarter-mode operation, featuring a low profile and ease of integration. Nevertheless, they can only cover the 28 (27.5–29.5) and 38 GHz (37–38.6 GHz) subbands by individual SIW modes separately.

Shared aperture antennas, such as a microstrip grid antenna forming the shared aperture with parasitic patches [13], a shared circular aperture antenna fed by combined ridge-groove gap waveguide technology [14], a differentially fed slot antenna loaded with a substrate-integrated dielectric resonator antenna for low- and high-frequency radiations [15], and an SIW slot array antenna which shares the aperture with a patch antenna [16], have been proposed to implement the desired LB and UB. Also, these can only achieve a limited operating bandwidth and cannot meet the requirements simultaneously, as the fractional bandwidth varies from 2.77% to 15.65% and 1.77% to 16.7%, respectively, at their lower and upper operation bands. In addition, the structures in [15], [16], and [17] were designed with a large frequency ratio operating at microwave and mm-Wave bands, while that of [14] had a rather bulky full-metal body.

On the other hand, an alternative solution is to cover the 5G New Radio FR2 bands at the Ka-band from 24.25 to 40 GHz

Manuscript received 2 May 2022; revised 10 July 2022; accepted 3 August 2022. Date of publication 30 September 2022; date of current version 22 December 2022. This work was supported in part by Nokia Corporation Ltd., in part by the Academy of Finland through the 6G Flagship Program under Grant 346208, and in part by the Business Finland RF Sampo Project under Grant 2993/31/2021. The work of Jiangcheng Chen was supported in part by the Nokia Foundation and in part by the HPY Research Foundation. *(Corresponding author: Jiangcheng Chen.)*

The authors are with the Centre for Wireless Communications, University of Oulu, 90570 Oulu, Finland (e-mail: jiangcheng.chen@oulu.fi).

Color versions of one or more figures in this article are available at https://doi.org/10.1109/TAP.2022.3209217.

Digital Object Identifier 10.1109/TAP.2022.3209217

(49%) by a single broadband antenna with an impedance bandwidth as wide as approximately 49%. However, the reported wideband E-patch antenna [18], dipole antenna [19], and metasurface-based antennas [20] achieve bandwidth from 19% to 31%, which cannot satisfy the bandwidth requirement. The abovementioned dual-band and wideband antennas only realize a single polarization. For widening the bandwidth, there are in general two methods at microwave and mm-Wave bands: combining multimodes, e.g., with higher order modes by reconfiguring the antenna structure [21], [22], and stacking patches together without increasing the overall footprint [23], [24]. Still, their bandwidths up to 45.4% are lower than required, and most of these designs are only single-polarized.

The well-known wideband magnetoelectric (ME) dipole, which includes an electric (E) and a magnetic (M) dipole mode, has attracted significant attention since it was invented [25], [26]. The E dipole of this complementary source antenna typically comprises a pair of patches, while the M dipole is made up of a vertical shorted patch or aperture antenna [3], [27], [28], [29], [30], [31], [32], [33]. At mm-Wave bands, substrate-integrated gap-waveguide-fed ME dipoles [29], [30] obtained insufficient 29% and 25.8% operating bandwidths, respectively, with broadside radiation characteristics. Although wider bandwidths of 44.4% and 50% have been achieved [27], [31], ME dipole elements excited by L-shaped probes supported merely a single linearly polarized operation.

Three potential antennas have been demonstrated for the Ka-band in [3], [28], and [33] to obtain a dual-polarization bandwidth of 45%, 50%, and 52.9%, respectively. Nonetheless, they suffer from poor port-to-port isolation varying from 14 to 20 dB with an XPD of around 20 dB due to their single-ended and asymmetric feeding techniques. Meanwhile, asymmetric structures lead to the nonidentical performance of two orthogonal polarizations and asymmetric radiation patterns in a way that each polarization was required to be adjusted separately, which increased the design effort. To address these issues, the differential feed proposed in [34] and [35] can be adopted to keep the structure symmetrical. More importantly, the differential feed technique can suppress the surface waves [34].

This article presents a differential probe-fed cross-slotted patch with dual-polarization for 5G mm-Wave bands to realize more than 57% of impedance bandwidth and maintain stable radiation characteristics across the overall operating band. The proposed antenna operates as a complementary antenna that contains two E dipole modes and one M dipole mode rather than one single E dipole mode and one M dipole mode in traditional ME dipoles. In Section II, antenna designs of a single element, novelties of the design, and a 2×2 array for verification of mutual coupling are presented. The operating principle is clearly illustrated with the help of characteristic mode analysis (CMA) in Section III in which the E dipole modes and the M dipole mode are investigated separately. It is shown that the CMA helps to find a "hidden" higher order mode that has the potential to enhance the bandwidth. Moreover, it provides insights into the way to improve impedance matching by modifying the inherent reactance. The simulated and measured results and parametric studies based on the equivalent circuit of the proposed ME dipole are demonstrated in Section IV, followed by conclusions in Section V.

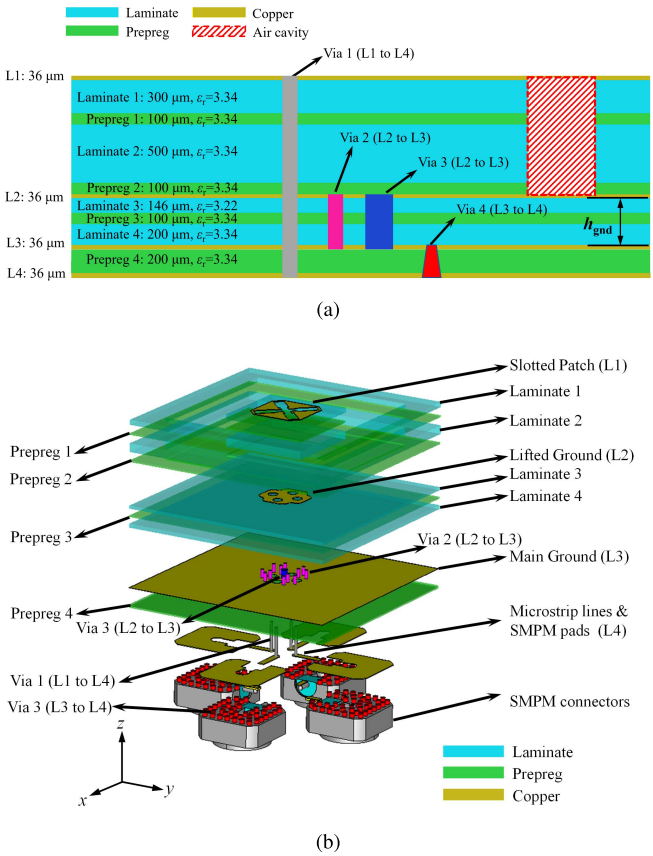

Fig. 1. Configuration of the proposed antenna: (a) PCB stack and (b) exploded view.

II. Antenna Design

A. Unit Cell

Fig. 1 illustrates the stack and exploded view of the proposed differentially driven dual-polarized broadband cross-slotted patch antenna, which consists of a cross-slotted octagonal radiation patch (L1), an additional lifted ground (LGND) (L2), the main ground (L3), and microstrip feedlines (L4). Panasonic Megtron 7 laminate and prepreg (bonding layer) are used for the stack. To be more precise, the octagonal patch (evolved from a rectangular patch) with a cross slot is situated on L1. The two orthogonal primary slots with the length of l_1 and the width of w_1, forming the cross slot, are loaded with two secondary slots at the short-circuited ends with the length of l_2 and the width of w_2, respectively, for the purpose of further impedance matching and resonance fine-tuning. It is noteworthy that the designed ME dipole can be regarded as a nonuniform-width polygonal ring patch antenna [36] in which the inner edges of the ring form the aperture serving as a slot antenna. The thick cross-like LGND is employed on L2 to tune the impedance matching and radiation gain for UB. The main ground plane is printed on L3 to isolate the antenna substrate and feedline substrate. Meanwhile, it serves as the reflector for the radiating patch as well. Four through-hole plated vias (Via 1 with a radius of 0.1 mm)—the feeding

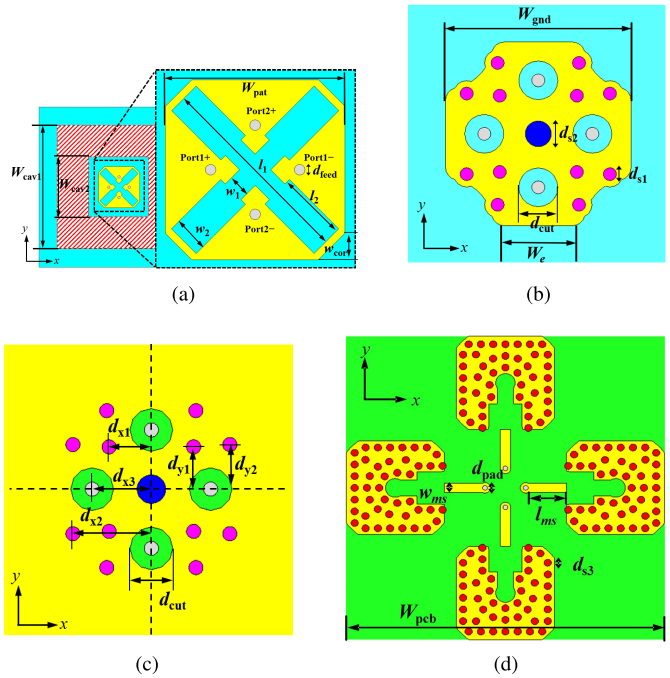

Fig. 2. Description of the layers in the proposed antenna: (a) Layer 1 (L1), (b) Layer 2 (L2), (c) Layer 3 (L3), and (d) Layer 4 (L4, bottom view).

probes—connect the patch on L1 to one end of the microstrip feedlines on L4, and they are grouped into two differential pairs in opposite locations. Another end of the feedline is fed by a high-frequency mini sub miniature push-on (Mini-SMP) connector. Furthermore, a vertical transition [37] is implemented as the quasi-coaxial line between the LGND on L2 and the main ground on L3 using shorting vias, Vias 2 and 3, to encircle the feeding pins to eliminate the parallel-plate mode. To get rid of the surface wave modes, an air cavity [38] with a depth of 1 mm from the top layer is utilized by removing away the substrate surrounding the 5×5 mm^2 unit cell in the large PCB for the unit cell prototype illustrated by the dashed red box in Figs. 1(a) and 2(a). Via 4 is a blind laser via with a diameter of 250 μm, while Vias 2 and 3 are buried vias.

In Fig. 2, the detailed configuration of each layer is presented along with dimensions. The radiating patch with a step-impedance cross slot shown in Fig. 2(a) is printed on the top layer and fed by the differential pairs (feeding pins) Port 1 and Port 2 along the symmetry planes xz and yz placed near the inner edges of the deformed ring patch, which can excite three desired modes for wideband characteristics. Fig. 2(b) and (c) depicts the 5×5 mm^2 unit cell area of L2 and L3, respectively. As shown, the vertical transition incorporates shorting vias Via 2 and 3 that encompass the feeding probes, forming the quasi-coaxial line. Four concentric circular holes with a radius of 0.3 mm are made in the ground plane for the corresponding four feeding pins. The lifted GND is evolved from a square shape by cutting off its four corners, and its size is smaller than that of the radiating patch. Together, these two result in the reduction and cancellation of the large capacitive reactance and, thereby, improve the impedance matching. Being smaller than the patch, the LGND will primarily affect the operation of the higher order mode in terms of matching and radiation characteristics, and only slightly detune the resonance of the first desired mode. The pads of SMPM coaxial connectors and feedlines are presented in Fig. 2(d). Both the SMPM connector and microstrip feedlines have a characteristic impedance of 50 Ω. The optimized design parameters are listed in Table I.

TABLE I
PARAMETERS OF THE PROPOSED CROSS-SLOTTED PATCH ANTENNA

Param.	W_{pat}	W_{gnd}	W_{cav1}	W_{cav2}	W_e	W_{pcb}	W_{array}
Value (mm)	3.35	2.85	10	5	1.04	13	36
Param.	w_1	w_2	w_{ms}	w_{cor}	l_1	l_2	l_{ms}
Value (mm)	0.41	0.65	0.4	0.495	3.76	1.3	0.4
Param.	d_{s1}	d_{s2}	d_{s3}	d_{x1}	d_{x2}	d_{x3}	d_{cut}
Value (mm)	0.2	0.4	0.25	0.59	0.625	0.83	0.6
Param.	d_{y1}	d_{y2}	d_{pad}	d_{feed}	h_{gnd}		
Value (mm)	0.59	1.1	0.44	0.2	0.446		

B. Main Antenna Features

Compared with reported dual-polarized ME dipole and ring patch antennas, the main novelties/features of the proposed antenna can be described in the following way.

1) Against only one electric dipole mode and one magnetic dipole mode of a traditional ME dipole in [3], [27], [28], [29], [30], [31], and [33], the proposed ME dipole contains two electric dipole modes and one magnetic dipole mode, providing a broadened operating bandwidth. To the best of our knowledge, the CMA is applied for the first time to the analysis of the ME dipole operation. With CMA, an additional electric dipole mode is identified, and its matching is improved based on the provided reactance insights. What is more, the magnitudes of the radiated power of the electric dipoles are shown numerically to be comparable with that of the magnetic dipole.
2) In contrast with the endfire radiation pattern of the higher order TM_{31} mode of a conventional ring patch or octagonal patch antenna, the proposed antenna has a broadside pattern favoring the formation of a complementary antenna at the UB. Moreover, the proposed antenna reduces the resonance of the TM_{31} mode of the conventional ring patch antenna by folding the current distributions. Thus, it shrinks the separation between the slot mode and TM_{31} mode resonance, and moves those resonances closer to each other.
3) Due to the symmetrical differential feed structure, each mode provides a stable and symmetrical radiation pattern, and in turn, the resultant antenna with combined modes has stable and symmetrical radiation property across the whole operating band. Furthermore, high port-to-port isolation and XPD are obtained due to the symmetrical feeding compared with traditional single-endedly fed ME dipoles.

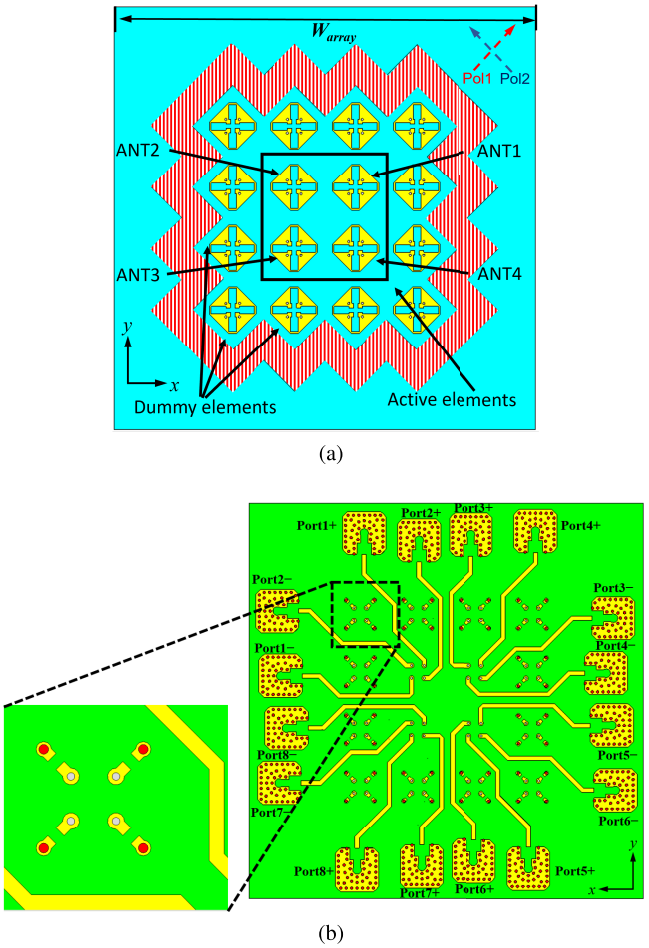

Fig. 3. Configuration of the 2 × 2 array: (a) top view and (b) bottom view.

4) The LGND acts as a tuning stub, and it is employed to resonate the TM_{31} mode by canceling the capacitive reactance of the natural impedance behavior, thereby improving the impedance matching and gain. More importantly, with this added discontinuity on the main ground plane, three resonances of the proposed antenna can be tuned independently.

C. 2 × 2 Array

To show the array capability of the proposed unit cell, a planar 2 × 2 array with ±45° slanted polarization shown in Fig. 3 is constructed. The four active elements are fed with individual differential pairs instead of a corporate feeding network to assess the mutual coupling between elements. The 0.57-λ_0 spacing at 32 GHz between unit cells is selected to compromise between grating lobe performance and the room needed to accommodate 16 SMPM connectors and feed lines. The unit cells in the 2 × 2 array follow the single-element design apart from slight modifications for matching purposes.

It is indicated in Fig. 3(a) that 12 dummy elements with 50 Ω terminations are added to each end of the through-vias, encircling the central four active elements to overcome the edge effects [39] of the 2 × 2 array on a large ground plane. In comparison with the single-ended antenna, amplitude and phase imbalance may occur without dummies in the case of a differentially fed antenna. Likewise, the air cavity (see the red dashed box) employed in the single-element design is also leveraged into the array to remove the unwanted substrate modes. Fig. 3(b) illustrates the feeding network of the four active elements and the terminations of 12 dummy elements. In total, 16 rotationally symmetric 50 Ω feed lines (having roughly equal electrical lengths) connect to the respective inputs of the feeding probes of four differential-fed dual-polarized antenna elements.

III. Operation Principle

The operation principle is studied using the theory of characteristic modes (TCM) [40] to shed insights into the natural behavior (resonances, current distributions, and radiation properties) of the electric dipole modes and the magnetic dipole mode of the proposed complementary antenna individually without any excitations. The aim is to find modes with desired resonance and broadside radiation characteristics and then to look for optimal feeding locations and techniques to combine the desired modes for broadband operation. A simplified model of the proposed antenna, as shown in the inset of Fig. 4(b), was used for CMA without feeding substrate and microstrip feed lines. Feed probes are kept in place for more accurate modal analysis as the eigencurrent, and its induced radiation also contributes to the modal performance of the antenna [41].

A. Characteristic Mode Analysis

The CMA was carried out mainly in CST Studio Suite by using the integral equation solver for electric CMs and partially in FEKO for the magnetic CM study to gain more insight into the aperture mode contribution to the total radiation. The boundary settings were the same as in [42]. In all modal analyses, the ground plane on layer L3 was made infinitely large, and a slot (or aperture) was embedded into an infinite conducting plane on layer L1, implemented by planar Green's function in the Method of Moment (MoM) code of FEKO. All metal planes were made of perfect electric conductors (PECs).

In view of both electric and magnetic eigencurrents existing in the magnetic CM, applying combined characteristic modes (CCMs) to the CMA for the proposed patch with aperture is needed because the eigenmodes of the patch loaded with a slot consist not only of purely magnetic eigencurrents over the slot but also of electric eigencurrents flowing on the conducting probes. In addition, it is ambiguous how the slot mode and electric current mode contribute to the total radiation by using purely electric CMs [43]. The CCMs are formulated as [44]

$$[X]\begin{bmatrix} J_n \\ jM_n \end{bmatrix} = \lambda_n^o [R]\begin{bmatrix} J_n \\ jM_n \end{bmatrix} \tag{1}$$

where $[X]$ and $[R]$ correspond to the imaginary and real parts of the MoM impedance matrix $[Z]$; λ_n^o is the nth eigenvalue for the eigencurrent $[J_n \;\; jM_n]^T$ of the nth CM. Note that the superscript "o" represents purely electric (e), purely magnetic (m), or CCMs. When only an electric or magnetic current exists on the antenna, the CCMs reduce to purely electric or magnetic characteristic modes.

The expansion of total electric and magnetic currents on the body is described as

$$\begin{bmatrix} J_t \\ jM_t \end{bmatrix} = \sum_n a_n \begin{bmatrix} J_n \\ jM_n \end{bmatrix} = \sum_n \frac{\left\langle \begin{bmatrix} J_n \\ jM_n \end{bmatrix}, \begin{bmatrix} E_i \\ jH_i \end{bmatrix} \right\rangle}{1 + j\lambda_n^c} \begin{bmatrix} J_n \\ jM_n \end{bmatrix} \tag{2}$$

where a_n denotes the modal weighting coefficients (MWCs) and $[E_i \quad jH_i]^T$ represent the incident fields. In addition to MWCs, the parameters modal significance (MS) and the characteristic angle (CA) are also critical for the CMA in this work, and they are defined as

$$\mathrm{MS}_n^o = 1/\left|1 + j\lambda_n^o\right| \tag{3}$$

$$\mathrm{CA}_n^o = 180^\circ - \arctan\left(\lambda_n^o\right). \tag{4}$$

When the eigenvalue $\lambda_n^o(f_n^o) = 0$ at a certain resonance frequency f_n^o, $\mathrm{MS}_n^o(f_n^o) = 1$, and $\mathrm{CA}_n^o(f_n^o) = 180^\circ$, respectively. A CM is inductive when $90^\circ < \mathrm{CA}_n^o < 180^\circ$ and capacitive when $180^\circ < \mathrm{CA}_n^o < 270^\circ$ In addition, a mode is considered significant when $\mathrm{MS}_n^o \geq 1/(2)^{1/2}$ ($\approx$0.707) [45].

The normalized MWC (normalized MWC or b_n) indicates how strongly a certain mode is excited by the differential feed and can be computed by [46]

$$\rho_{\mathrm{tot},n} = \frac{\frac{1}{2Z_0} \oiint_{S'\to\infty} \vec{E}_{\mathrm{tot}} \cdot \vec{E}_n^* \mathrm{d}S}{\sqrt{\frac{1}{2Z_0} \oiint_{S'\to\infty} \left|\vec{E}_{\mathrm{tot}}\right|^2 \mathrm{d}S} \sqrt{\frac{1}{2Z_0} \oiint_{S'\to\infty} \left|\vec{E}_n\right|^2 \mathrm{d}S}} = \frac{a_n}{\sqrt{P_{\mathrm{rad}}}} = b_n. \tag{5}$$

Computationally, the MWC relates to the well-known envelope correlation coefficient (ECC) used with MIMO antennas.

B. Modal Significance and Characteristic Angles

Fig. 4(a) and (b) shows the MS and CA of the proposed antenna element, respectively, compared with those of the antenna without the LGND. Only the first several modes with the highest MS magnitudes sorted at 31 GHz are selected and presented. For pairs of degenerate modes (J_1/J_2, J_4/J_5, and CCM_1/CCM_2), the curves largely overlap because the antenna is rotationally symmetric. Hence, only one mode is shown for clarity. Compared to the case without the feeding probe, the modal behavior (current distribution) changes due to the probe itself [41]. Therefore, the feeding probes are included and shorted to the main ground plane in the present analysis.

To better understand the operating principle and evolution of the proposed slotted patch, the CMA was first performed without the LGND. MS results without LGND indicate that, within and close to the band of interest (Ka-band), there are four significant modes: a degenerate electric current mode pair J_1/J_2, a degenerate combined mode pair CCM_1/CCM_2, mode J_3, and combined mode CCM_3, with another degenerate mode pair J_4/J_5 for which the MS is below 0.707 due to the natural capacitive reactance of this mode with a CA greater than 180°. After the LGND is introduced, the added inductance caused by the LGND cancels the original capacitance of mode J_4/J_5, and hence, the mode becomes significant from 35 GHz

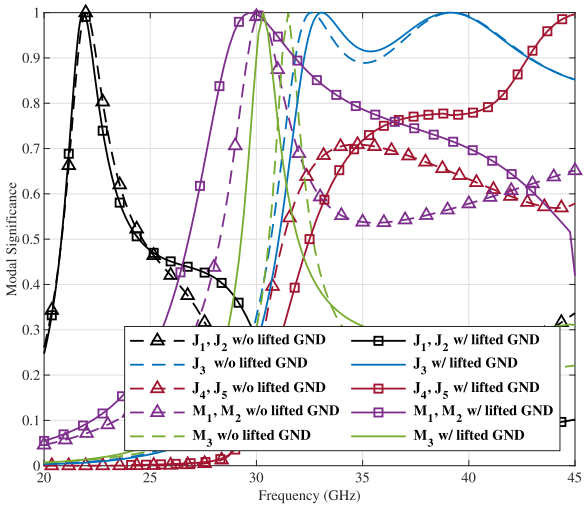

(a)

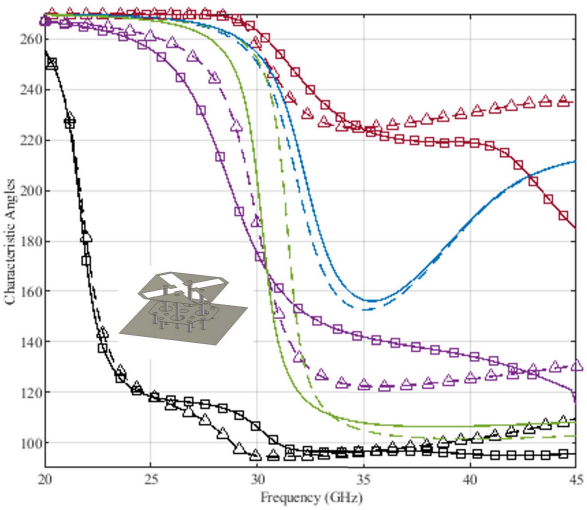

(b)

Fig. 4. CMA: (a) MS and (b) CA with an inset of the simplified model for CMA. Both figures share the same legends.

onward and resonates at 45.8 GHz. This reveals that J_4/J_5 is a potential mode for widening the bandwidth at the UB. In other words, MS and CA play a vital role in finding significant and potential modes that can be utilized and also suggest how to modify the natural reactance of J_4/J_5 to make it resonant. To elaborate, the introduced LGND works as a short-circuited reactance stub exerting a minor inductive effect on mode J_1/J_2 and a strong inductive effect on J_4/J_5 above approximately 35 GHz. Also, it causes a capacitive effect (increased CA above 30 GHz) between two parallel plates on the aperture mode CCM_1/CCM_2, as demonstrated in [47], and, at the same time, makes the slope of CA around the resonance less steep. This indicates a broadened bandwidth potential.

In addition, the LGND has minor effects on the other modes and an almost negligible effect on mode J_1/J_2 around its resonance of 22.8 GHz. To sum up, the LGND predominantly varies the reactance of mode J_4/J_5 above 35 GHz with a strong

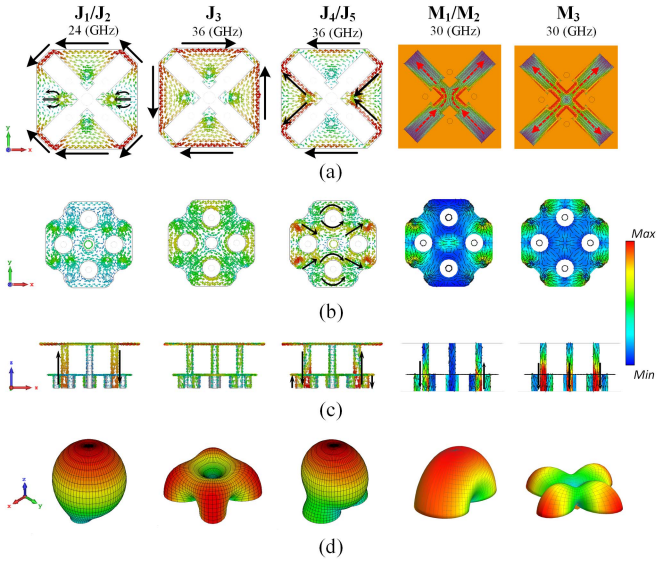

Fig. 5. Modal results of the tracked significant modes: (a) top view, (b) side view, (c) side view of modal current distributions, and (d) their corresponding modal fields at 24, 36, 36, 30, and 30 GHz, respectively. Parts (a)–(c) are given in A/m, and part (d) is in V.

inductive loading effect, while it has limited effects on other modes and their radiation properties.

On the other hand, the CA results also imply that the excitation phase difference between CCM_1/CCM_2 and J_1/J_2, and between J_4/J_5 and CCM_1/CCM_2 would be around 90°, e.g., in the vicinity of 28 and 34 GHz, respectively. To be more precise, while the phase of J_1/J_2 leads that of CCM_1/CCM_2, the phase of J_4/J_5 lags that of CCM_1/CCM_2.

C. Modal Currents and Fields

Following the MS and CA results, their associated modal currents and fields are presented in Fig. 5(a)–(d). Since the modal current is identical to its orthogonal degenerate mode but with a rotation of 90° due to structural symmetry, modal currents and fields of only one mode in each degenerate mode pair will be shown in the rest of this article.

It can be seen from the electric current distributions (represented by black arrows) on the top surface in Fig. 5(a) that the modes J_1/J_2 and J_4/J_5 can be recognized as quasi-TM_{12} and quasi-TM_{31}, resembling those of a traditional ring patch antenna [36], [48]. Furthermore, the aperture mode CCM_1/CCM_2 can be regarded as a synthesis of two orthogonal line slots, and its radiation is accounted for by the magnetic currents (denoted by red arrows). More importantly, there exists an intense and in-phase current distribution flowing along the whole surface of the LGND for mode J_4/J_5 shown in Fig. 5(b), together with the vertical currents on the shorting pins. The introduced LGND acts as the reactance stub providing a new current path that generates an enhanced stored magnetic energy within the cavity of the slotted patch. Therefore, the antenna with LGND has an increased inductance as previously revealed by the CA results. This inserted discontinuity technique (LGND) on the main ground plane is analogous to the tuning screw/post-matching technique of conventional rectangular waveguides [49], where the shunt susceptance is controlled by the length of the post and the inductance is proportional to the height [50].

Fig. 5(c) reveals the current distributions on one pair of the feeding probes. For modes J_1/J_2, J_4/J_5, and CCM_1/CCM_2, the currents are 180° out of phase. These odd-mode modal currents indicate that the optimal feeding location is at the probe base, and they can be excited by a differential pair. In contrast, mode CCM_3 illustrates in-phase current distributions, and it can be excited by a common-mode input. On the other hand, mode J_3 shows a weak current density on the probes, and in turn, no excitation on the probes can effectively excite this mode. The modal fields in Fig. 5(d) show that there are three desired modes, J_1/J_2, J_4/J_5, and CCM_1/CCM_2, with favorable broadside radiation characteristics, while the other two modes have endfire radiation.

In conclusion, the three desired modes with high MS magnitudes have broadside radiation and can be fed with a differential input at the probe base. The slot mode resonance remains similar when the infinite conducting plane carrying the slot is made finite [51]. Due to the orthogonality of characteristic modes, each desired degenerate mode pair used for dual-polarization operation achieves high port-to-port isolation.

To further investigate the wideband operation of the proposed antenna, the modal current distributions and modal radiation patterns of three desired modes evolving across five discrete frequencies are illustrated in Fig. 6(a) and (b), respectively. With the gradual change of the modal current distributions, the corresponding induced modal radiation patterns vary accordingly. To recapitulate briefly, the in-phase currents of J_1/J_2 and J_4/J_5 along the x-axis at LB and UB, respectively, give rise to the boresight radiation pattern, while out-of-phase current distributions along the vertical symmetric plane lead to endfire like radiation patterns. Furthermore, the slot mode maintains stable modal magnetic current distributions across the whole frequency range. As a result, the modal radiation pattern contributed by the respective modal current appears to be stable with a consistent broadside radiation property.

Also, it can be seen from Fig. 6(a) that the magnetic current distribution remains stable though the MS and CA in Fig. 4(a) and (b) vary with frequency. This is because at resonance the magnetic dipole is operating at fundamental half-wavelength dipole mode, and the current distribution of the mode remains in phase along the dipole length when the magnetic dipole becomes electrically smaller or larger unless a higher order mode, e.g., one-wavelength mode arises, which is analogous to an electric dipole. Moreover, with the help of CA, the variation of MS with frequency indicates the variation of the stored electric and magnetic energy of the associated modes. Although the current distribution is in-phase for the fundamental dipole mode, the reactive power changes over frequency from capacitive to inductive around resonance.

The electric CM analysis for a slotted patch shows that the current is perturbed by the introduced slot as the aperture interacts and couples with the original electric characteristic modes. Therefore, the CMs of either the aperture or patch present a current distribution combination of both aperture and patch modes instead of independent current modes analyzed by

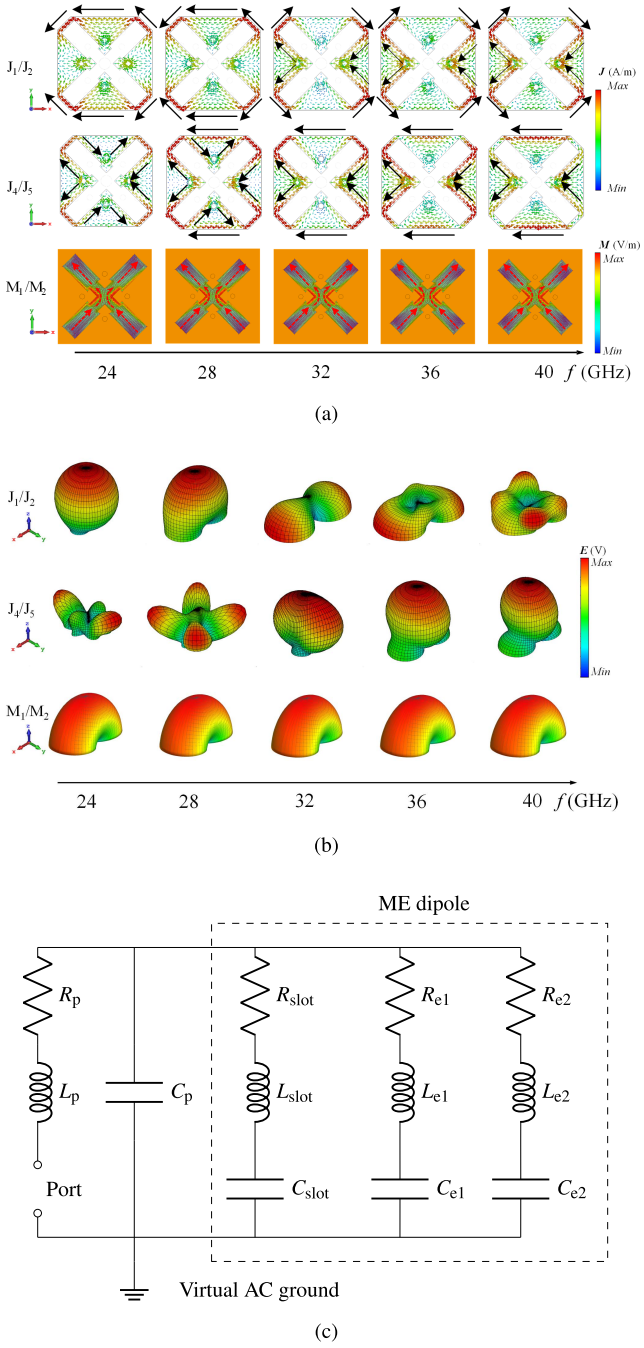

Fig. 6. (a) Modal current distributions and (b) modal radiation fields of three desired modes across the frequencies of interest and (c) corresponding equivalent circuit model for the proposed ME dipole.

merely the electric CM. Thus, the magnetic CM is required to provide more insight into the currents and radiation contributed by the aperture mode only. In addition, differing from the strong coupling between patch and aperture modes of the slotted patch in [52], the calculated correlation between J_1/J_2 and CCM_1/CCM_2 at 24 GHz and J_4/J_5 and CCM_1/CCM_2 by (5) at 40 GHz is only 28% and 32%, respectively, revealing low coupling and interaction between the patch modes (purely electric current) and aperture mode (CCMs). This is because the cross-slot is rotated by 45° from the x- and y-axes so that the current maxima at the ends of the slot will be aligned with the current minima of an unslotted patch at the

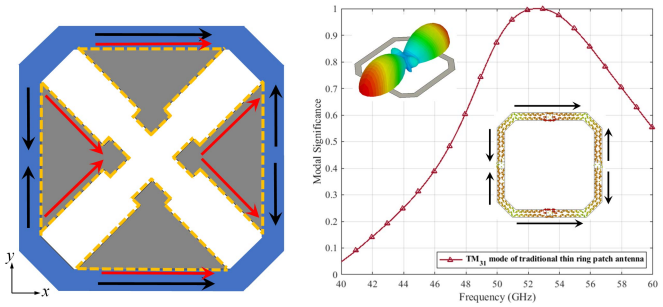

Fig. 7. (a) Modal currents in the geometry of a traditional thin ring patch (black arrows) compared to the proposed patch (red arrows) and (b) MS with insets of modal field and current distributions.

corners of the patch. In other words, the radiation of J_1/J_2 and J_4/J_5 regarded as electric dipoles is mainly contributed by the electric currents of the patch itself, while the magnetic currents of CCM_1/CCM_2 considered as a magnetic dipole are responsible for the aperture mode radiation. The radiation patterns of selected modes (E and M dipoles) in Figs. 5 and 6 have a linear polarization in the x-direction.

D. Combining Desired Modes for Complementary Operation

Based on the observations above, by combining these three modes, we would obtain a complementary antenna with broadband and stable broadside radiation at the desired frequency range. Specifically, the combination of J_1/J_2 and CCM_1/CCM_2 at LB and the mixture of J_4/J_5 and CCM_1/CCM_2 at UB together generate the complementary antenna operation. The corresponding equivalent circuit model for the proposed complementary or ME dipole antenna [26] is then developed in Fig. 6(c) in accordance with that in [53] owing to the odd-mode excitation of a symmetrical network and the fact that a symmetric plane can account for a short circuit (virtual ac GND) of the bisection. The equivalent circuit model of three series resonant circuits in parallel results from the fact that the equivalent circuit for a structure is the parallel combination of individual modal circuits (which themselves are series resonances) [47]. Note that the magnetic dipole mode in this work is represented by a series RLC resonant circuit instead of the parallel resonant circuit in [26]. Based on the transmission line theory [54], parallel and series types of resonances can be achieved using short-circuited transmission lines of length $\lambda/4$ and $\lambda/2$, respectively. In [26], the magnetic dipole is implemented by a $\lambda/4$ shorted patch, while the length of the electrical path in this work is about $\lambda/2$ from the port to the virtual ground along the folded slot. R_p, L_p, and C_p denote the equivalent resistance, inductance, and capacitance resulting from the feeding probes, respectively. $R_{e1/e2/slot}$, $L_{e1/e2/slot}$, and $C_{e1/e2/slot}$ denote the equivalent resistance, inductance, and capacitance of J_1/J_2, J_4/J_5, and the aperture mode, respectively.

Fig. 7(a) shows how the radiation property of the higher order quasi-TM_{31} mode of the proposed nonuniform-width octagonal ring patch differs from a corresponding traditional ring patch. The modal performance is also investigated in Fig. 7(b). The black arrows flowing along the blue rim represent the electric current distribution of a traditional ring

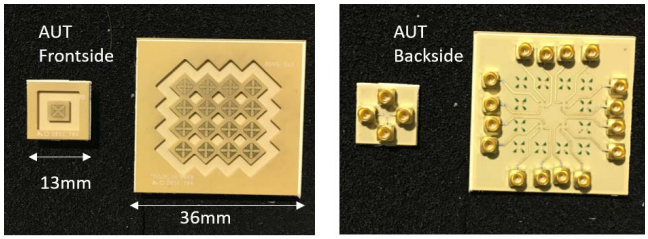

(a)

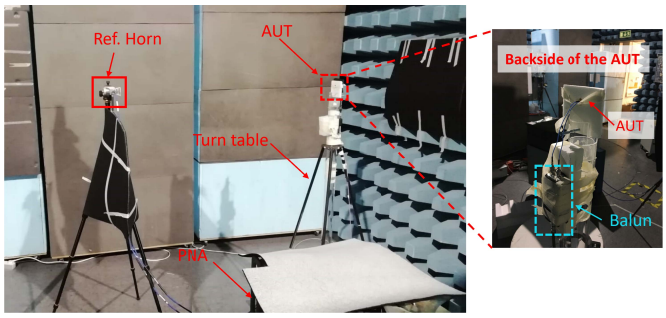

(b)

Fig. 8. Photographs of (a) single antenna element (left) and 2 × 2 array (right) and (b) used measurement setup.

patch, and the red arrows flowing along the yellow frames illustrate that of the proposed patch. As shown, adding four triangle-like patches (enclosed by the yellow dashed lines) to the traditional octagonal ring patch folds the current path along the perimeter of the azimuth plane. In turn, the first and third current cycles along the vertical rim move to the inner edges of the ring, thereby making the current density of the modified patch akin to that of a folded dipole antenna, as illustrated in Fig. 5(a). As a consequence, the radiation pattern induced by the current distribution features broadside radiation for the higher order mode, while the traditional ring patch has an endfire radiation characteristic due to the out-of-phase current distribution in the vertical rim. More importantly, the natural resonance of the higher order mode TM_{31} decreases from around 52.8 to 45.8 GHz, thus reducing the resonance ratio of TM_{31} to the slot mode and TM_{12}. This facilitates combining them with the slot mode resonance for broadband operation.

IV. Simulation and Measurement Results

To validate the design, the single element and 2 × 2 array shown in Fig. 8(a) were fabricated and measured. The *S*-parameter measurements were carried out using a Keysight N5247B PNA-X network analyzer, and each port was connected to a Rosenberger 18S102-40ML5 SMPM connector on the antenna PCB through a coaxial cable. A thru–reflect–line (TRL) calibration kit [55] was used in the measurement as the connection between SMPM connectors and coaxial cable is not a standard interface for the PNA. With the TRL calibration technique, the reference plane of the port is moved closer to the antenna element, and the effects of the connector and feed line are deembedded. Time-domain gating was applied to the measured *S*-parameters since the long connection path and discontinuity from the antenna port to PNA port via connectors, adapters, and cables cause mismatch and a ringing

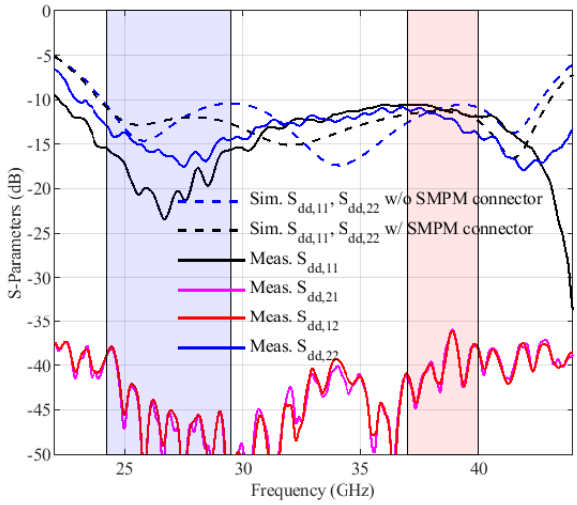

Fig. 9. Simulated and measured *S*-parameters for the single element.

effect [22]. Moreover, the differential mode *S*-parameters are calculated based on the technique described in [56].

The measurement setup for the radiation patterns is presented in Fig. 8(b). A low-permittivity Rohacell slab was placed on the post of the turntable to mount the antenna under test (AUT), and a standard gain horn antenna was used as the reference antenna. Absorbers (see the black blankets) were used to suppress multiple reflections from the environment. The distance between the AUT and reference horn was selected to be 1.2 m ($129\lambda_0$), which is in the far-field range of the measured prototypes. The radiation pattern of the single-element prototype was measured directly with a Marki BAL0067 mm-Wave balun. With the other three unit cells terminated to 50 Ω, the pattern of the array prototype was obtained by sequentially exciting each unit cell fed by coaxial cables. Thereafter, the four individual patterns were combined to obtain the array pattern radiating at boresight by summing the measured four field vectors with equal phase and amplitude weighting in MATLAB, as implemented in [57].

A. Single Element

The simulated and measured *S*-parameters of the single element are presented in Fig. 9. A decent agreement between the simulation and measurement results is obtained. Depicted by the light blue and red shadowed areas, the matching achieves a −10 dB level across the desired LB and UB, covering a bandwidth of more than 50%. The SMPM connector slightly affects the matching because of soldering inaccuracies and the discontinuity in the center conductor to microstrip transition.

The three resonances are slightly mistuned from those given by the CMA because of the feed structure. Due to differential feeding, the two orthogonal polarizations of a symmetrical antenna have ideally an infinite isolation. Thus, the simulated mutual coupling is not shown. Fabrication tolerances introduced some asymmetry into the antenna prototype, thereby degrading the ideal isolation. Still, the mutual coupling of the two polarizations is below −36 dB across the frequencies of interest even when accounting for fabrication tolerances.

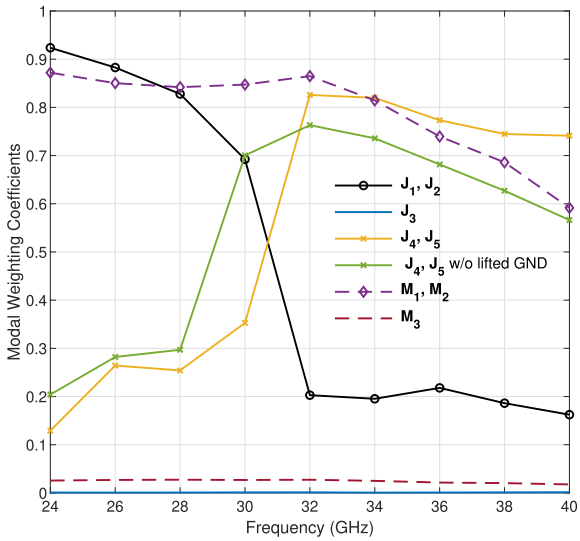

Fig. 10. Calculated normalized MWCs for excitation with the differential feed.

The simulated radiation and total efficiencies are above 93% and 87% within the desired band, respectively.

From the normalized MWC calculated by (5) in Fig. 10, it is evident that, at LB and UB, J_1/J_2 and J_4/J_5 are strongly excited, respectively, as high MWCs are obtained for each mode. J_1/J_2 and J_4/J_5, in turn, contribute to the total radiation at LB and UB alternately. In comparison with J_4/J_5 without the LGND, the magnitude of the MWC is relatively higher for J_4/J_5 with the LGND since the MS magnitude is higher, and the intrinsic coupling capability to the differential source is stronger as well. Moreover, given that a high MWC is witnessed across the entire observed frequency range, the slot mode CCM_1/CCM_2 has a rather constant contribution to the total radiation, and at a center frequency around 31 GHz, the aperture mode contributes mostly with less and equal contribution from the other two modes.

The undesired modes have MWCs close to zero and will not be excited effectively. On top of that, Fig. 10 reveals that J_1/J_2 has comparable boresight radiated power contributions of electric and magnetic dipoles from J_1/J_2 and CCM_1/CCM_2 at LB and J_4/J_5 and CCM_1/CCM_2 at UB separately, as a result of similar magnitudes of b_n^2 [46], which indicates the percentage that a mode contributes to the total radiation. It is interesting to note that the magnetic dipole mode performing as a slot resonator provides a band-stop filtering function and suppresses the radiation created by the electric dipole modes around the center frequency. Meanwhile, the slot itself, acting as a radiator, contributes to the radiation.

To illustrate the operation principle of the ME dipole, the current and field distributions of the proposed antenna are shown in Fig. 11(a)–(d). The magnetic current is expressed as $\vec{M} = -\vec{n} \times \vec{E}_s$, where $\vec{n}$ and $\vec{E}_s$ are the normal vector and tangential electric fields on the aperture surface, respectively. Fig. 11(a) and (c) illustrates the driven current distributions with the differential probe feeding, showing that the desired quasi-TM_{12} (J_1/J_2) and quasi-TM_{31} (J_4/J_5) modes and the aperture mode are successfully excited. At time instants $t = 0$ in Fig. 11(a) and $t = T/4$ in Fig. 11(c), the electric currents on the inner edges of the nonuniform ring patch reach maxima separately, which reveals that the slot antenna mode is strongly excited. At the same time instants, the fringing fields of the quasi-TM_{12} and quasi-TM_{31} modes attain their maxima [see Fig. 11(b) and (d)]. At $t = T/4$ at 24 GHz and $t = 0$ at 37 GHz, the electric currents of the desired the quasi-TM_{12} and quasi-TM_{31} modes are at their maxima, respectively, indicating that the electric dipoles in the x-direction are efficiently excited. Meanwhile, the aperture fields of the magnetic dipole in the y-direction (resultant vector of magnetic currents) reach their maxima. Consequently, there is a 90° phase difference between two electric dipoles and the magnetic dipole, which means that they are excited alternately and radiate in-phase [58].

Furthermore, according to Fig. 10, the field magnitudes of the electric dipoles and magnetic dipoles are comparable in strength. Therefore, the combination of electric and magnetic dipoles with the same phase centers implies the radiation enhances in one direction and cancels in the opposite direction. Consequently, the proposed antenna incorporating the combination of three modes operates as a complementary antenna in which the mixture of quasi-TM_{12} and slot mode accounts for the LB operation, while that of quasi-TM_{31} and slot mode is responsible for the UB.

Simulated and measured radiation patterns at three discrete frequencies are shown in Fig. 12. In the azimuth plane, the measurement was carried out at an angular range of ±130° due to rotational limitations of the turntable. Again, the simulated cross-polar component is not shown here as it is extremely low (e.g., below −70 dB) with an ideal differential feed for a symmetric structure. It is explicitly illustrated that the simulated copolar patterns agree well with the measured ones. However, the cross-polar level becomes more noticeable compared with the simulated, which may result from fabrication tolerances that introduced some asymmetry into the antenna prototype, feed imbalance from coaxial cable effects, and measurement inaccuracies (e.g., AUT alignment). Radiation patterns are stable across the wide operating band, resulting from the ME dipole operation. In particular, the difference of the simulated 3 dB beamwidths of the E- and H-plane patterns is less than 5° from 25 to 34 GHz, as shown in Fig. 13, which indicates the symmetry between E- and H-plane patterns of the proposed complementary antenna. Moreover, both the simulated and measured XPD levels are high in boresight direction as expected because of the symmetric antenna design with XPD > 26 dB across the frequencies of interest. Slight discrepancies between the cross-polarizations of two orthogonal ports result from fabrication tolerances and prototype alignment during the measurements.

As seen in Fig. 13, the simulated and measured gains of the single element agree well across the whole operation band. The simulated gain ranges from 5.6 to 8.4 dBi, while the measured one fluctuates between 6.4 and 8.2 dBi. The dip in simulated gain near 28 GHz is due to diffraction effects at the outer edge of the PCB. As can be also seen from the figure, the measured gain from 26 to 38 GHz is higher than the simulated, which probably results from the fabrication tolerance of the air cavity size, inaccurate PCB

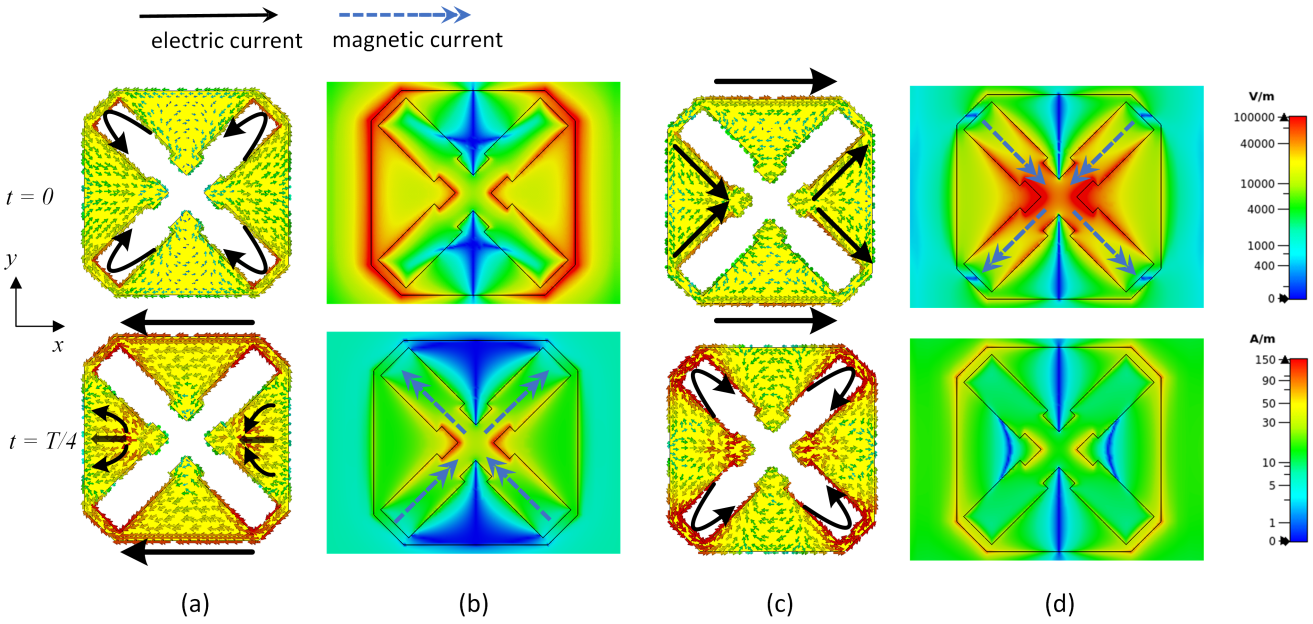

Fig. 11. ME dipole operation: (a) and (c) driven-mode current distributions at 24 and 37 GHz at different time instants, and (b) and (d) driven-mode electric field distributions at 24 and 37 GHz at different time instants.

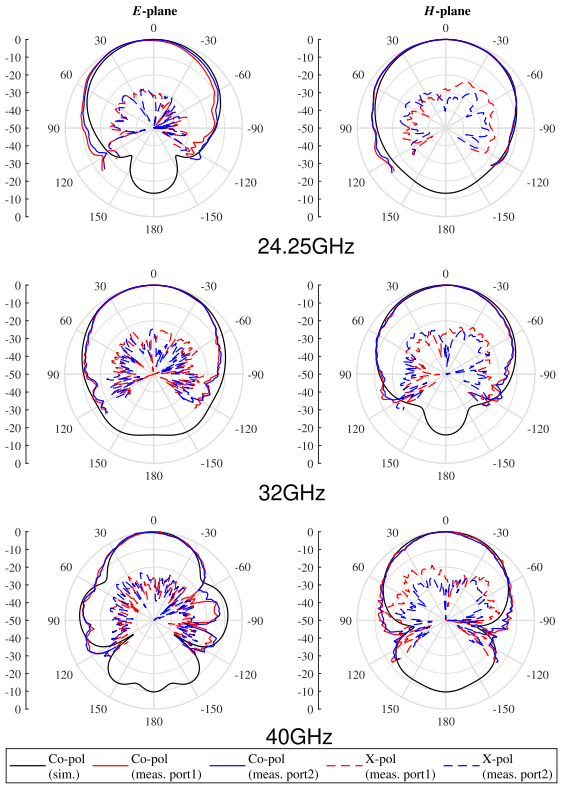

Fig. 12. Simulated and measured radiation patterns of the single element at 24.25, 32, and 40 GHz, respectively.

cutting, measurement inaccuracy, and loss compensation in postprocessing. The array gain is also presented in Fig. 13 and will be discussed in Section IV-C.

B. Parametric Study

The equivalent circuit shown in Fig. 6(c) is used to explain the effects of key parameters on the operation of

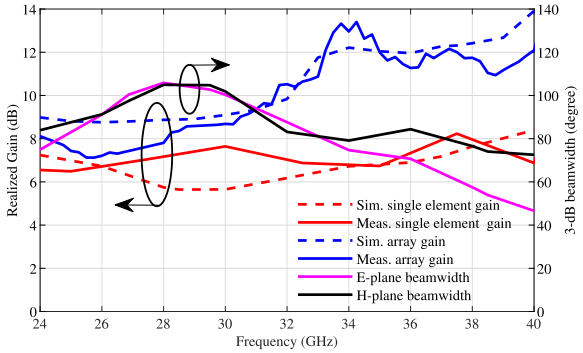

Fig. 13. Simulated and measured realized gain of the single element and 2 × 2 array, and simulated 3 dB beamwidth of the single element.

the single-element antenna case. These studies are performed by changing one parameter at a time, while others are kept constant.

1) Height of the Lifted Ground: In Fig. 14(a), the antenna shows two resonances without LGND at around 22.8 and 30 GHz. Initially, the antenna reactance without the LGND is capacitive ($L_{e2} < C_{e2}$), and increasing the height of the LGND makes the reactance more inductive. The equivalent inductance L_{e2} in Fig. 6(c) increases to cancel the equivalent capacitance C_{e2}. At a height of 0.446 mm, the reactance is zero, and a third resonance occurs around 41 GHz. The increased inductance is proportional to the height of the LGND [50]. Increasing the height of the LGND should reduce the probe capacitance C_p. The surface area of the parallel-plate capacitance formed by differential feeding probes is much smaller than that of the patch and ground, and thus, the effect of C_p is neglected when changing the LGND height for simplicity.

The antiresonance (AR) between two resonances originates from the interaction of two adjacent resonances of the same type of resonator [59]. Hence, the AR reveals the combination of two close resonances and provides an insight into

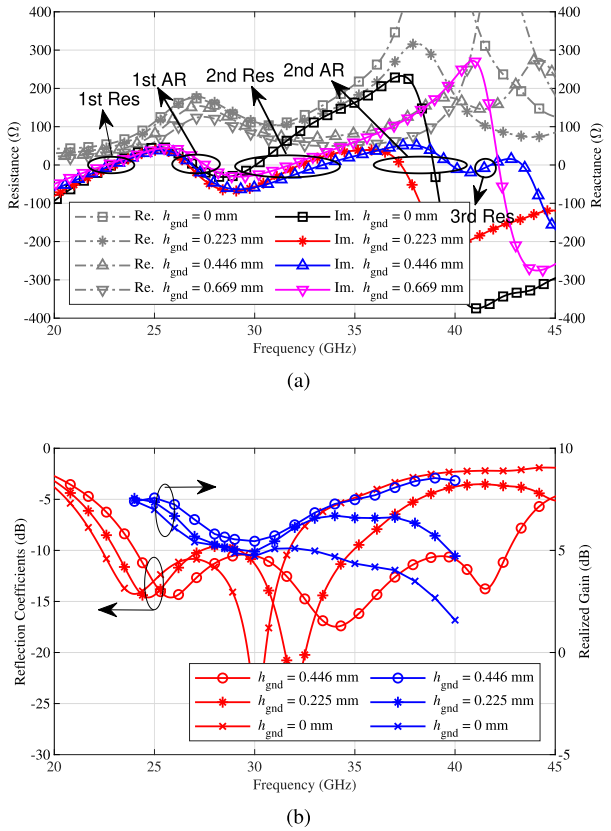

Fig. 14. Effects of the LGND height on (a) differential input impedance and (b) reflection coefficient and realized gain. Res and AR denote the resonance and antiresonance, respectively.

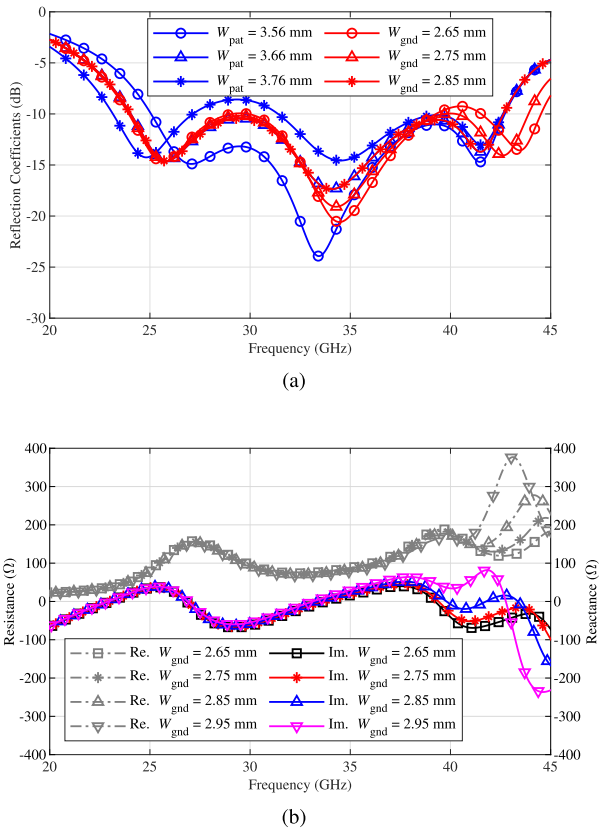

Fig. 15. Effect of the patch size W_{pat} and LGND size W_{gnd} on (a) reflection coefficient and (b) input impedance.

the broadband operation resulting from two merged modes. Interaction of the quasi-TM_{12} and slot modes generates the first AR, and the second AR results from the interaction of the second and third resonances. Interaction of different modes can also be seen from the reflection coefficients in Fig. 14(b): the impedance bandwidth increases from 34.5% to 57.1% due to the third resonance created by adding the LGND.

The slot-mode reactance of the modified antenna becomes more capacitive near 33 GHz due to the capacitive effect on this mode. Thus, the equivalent slot mode inductance L_{slot} decreases, and the frequency tunes upward. The LGND height can enhance the realized gain above 31 GHz, while the values remain stable at lower frequencies. Significant gain variation from 1.58 to 8.42 dBi is observed due to the LGND.

2) Size of the Patch and Lifted Ground: As seen in Fig. 15(a), the first resonance of the proposed antenna decreases as a larger octagonal patch lengthens the electric current path, which increases C_{e1} and L_{e1}. At the same time, the other two resonances remain stable. With a larger LGND area, the current path along this surface is longer, which enhances the local storage of magnetic energy in this resonant cavity [21], thereby increasing the inductance L_{e2} and capacitance C_{e2} caused by the LGND near 41 GHz, as shown in Fig. 15(b). Accordingly, the resonance of the quasi-TM_{31} mode moves to a lower frequency. The shape of the LGND is chamfered to control the reactance and improve the matching. When changing the size of the LGND, the input impedance of the first two resonant modes again remains unchanged.

3) Size of the First and Secondary Slots: A longer slot l_1 increases the equivalent inductance L_{slot} and capacitance C_{slot}, which causes a lower slot-mode resonance shown in Fig. 16(a). A similar effect on the slot-mode resonance is obtained by decreasing the length of the secondary slot l_2. A wider secondary slot (larger w_2) has lower equivalent parallel-plate capacitance than the primary slot, and the two slot sections can be considered as two parallel capacitors of slot width w_1 and w_2. Therefore, with shorter l_2 and longer l_1, the total capacitance C_{slot} of the slot-mode resonator increases, which shifts the resonance to a lower frequency. Changing the slot length l_1 allows controlling the resonance, but this also degrades the impedance matching. The slot length l_2 is a more favorable parameter to control the second resonance, while it also maintains a decent impedance matching. Furthermore, l_2 only affects the slot-mode resonance, while the other two resonances are unaffected.

As shown in Fig. 16(b), the smaller primary slot width w_1 lowers the resonance as the intense aperture field concentrates on the primary slot [see Fig. 11(b) and (d)]. This accounts for most of the slot capacitance C_{slot}; a smaller w_1 indicates a greater C_{slot}. Varying the secondary slot width w_2 has only a minor effect on the impedance matching and resonance of the slot mode since the aperture field is weak at the secondary slot. Thus, the resulting change to C_{slot} is small.

4) Observations: Based on the parametric studies, each of the resonances can be manipulated independently, indicating that the coupling between the slot mode and patch modes is relatively low. This proves that the modal current and radiation

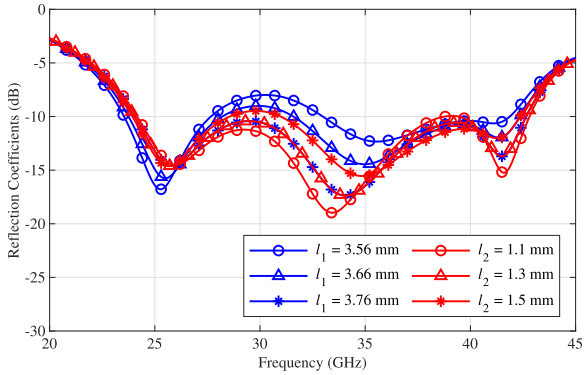

(a)

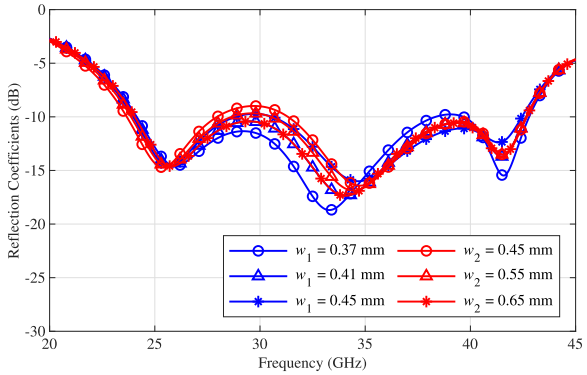

(b)

Fig. 16. Effect of the cross-shaped slot dimensions on the reflection coefficient: (a) length of first slot l_1 and secondary slot l_2, and (b) width of first slot w_1 and secondary slot w_2.

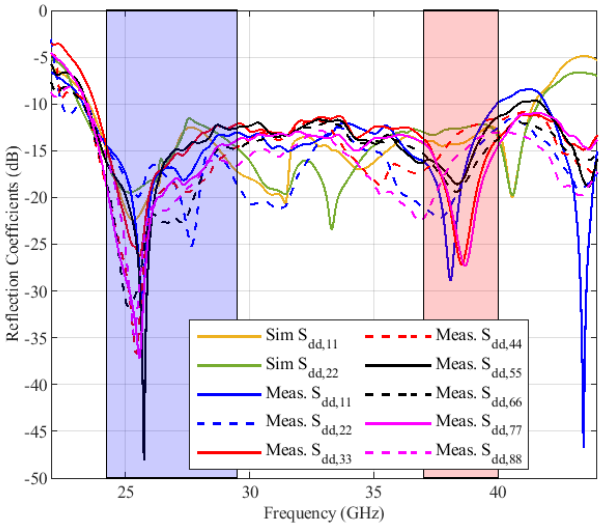

Fig. 17. Simulated and measured S-parameters for the unit cells of the 2×2 array.

of J_1/J_2 and J_4/J_5 mainly originate from electric current modes of the patch itself instead of the aperture mode for the electric CM study in Section III. For brevity, detailed parametric studies for the air cavity are not reported here. Without the cavity, the boresight radiation pattern is distorted/split, and the gain drops across the whole band for a large PCB with four SMPM connectors. This effect occurs because of strong

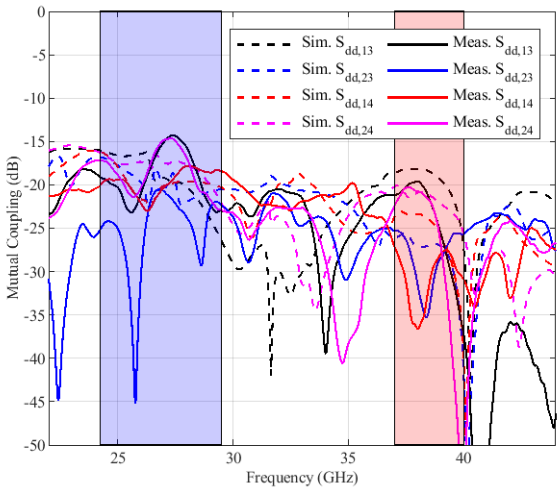

(a)

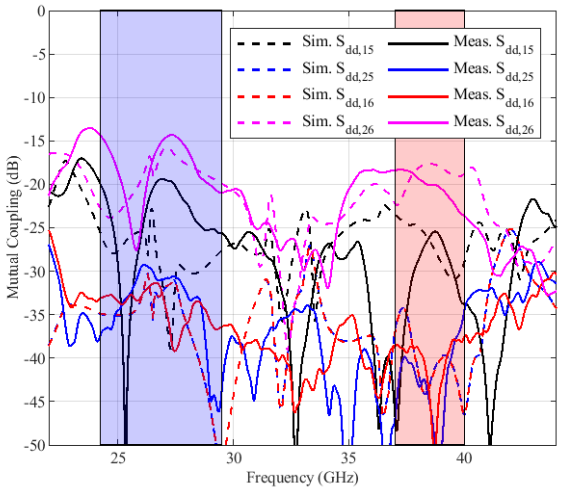

(b)

Fig. 18. Measured mutual coupling of the 2×2 array between (a) adjacent and (b) diagonal elements.

standing waves over the ground plane due to surface waves. By employing an air cavity, the deterioration can be mitigated.

C. 2×2 Array

Fig. 17 shows the reflection coefficients of the 2×2 array. Both the simulated and measured results have comparable levels and similar trends, which indicates that the impedance matching of both polarizations of all active elements can cover the desired frequency bands. Isolation among various polarizations of different active elements is illustrated in Fig. 18(a) and (b). Within the operation band, the mutual coupling level between adjacent elements, as shown in Fig. 18(a), is higher compared with that between diagonal elements, as shown in Fig. 18(b). Across the frequencies, the isolation remains better than 14 dB. Furthermore, the mutual coupling level between any two elements with the same polarization is stronger than that with orthogonal polarization. Generally, the measured coupling has a decent agreement with the simulated one. The isolation between diagonal elements is better

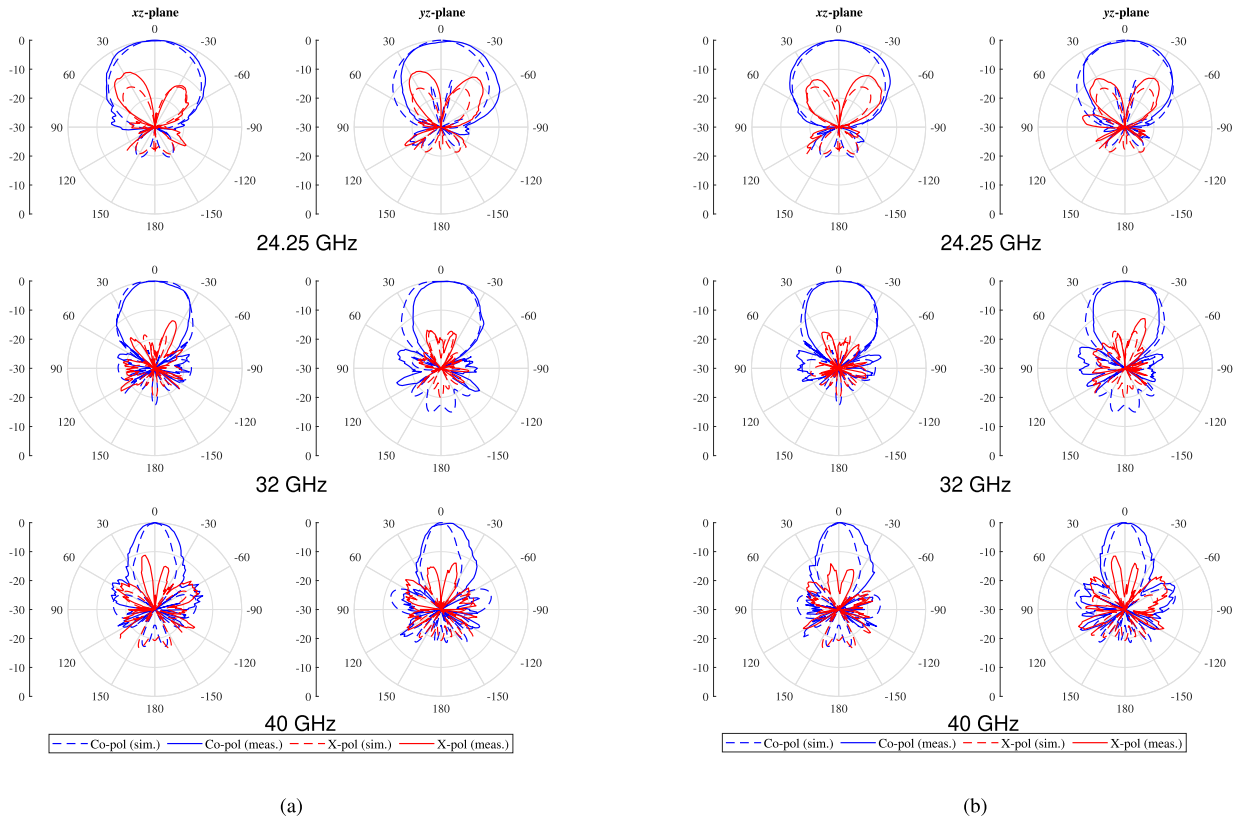

(a) (b)

Fig. 19. Simulated and measured radiation patterns of the 2 × 2 array: (a) Polarization 1 and (b) Polarization 2 at 24.25, 32, and 40 GHz, respectively.

TABLE II

COMPARISON BETWEEN THE PROPOSED ANTENNA AND STATE-OF-THE-ART mm-WAVE ANTENNA DESIGNS

Ref.	Antenna type	Techn.	ε_r	Size (Unit Cell) ($\lambda_0{}^3$)	Oper. band (GHz)	BW$^{(a)}$ (%)	Isol. (dB)	Polarization	XPD (dB)	$G_{\max}{}^{(b)}$ (dBi)	Array type
[3]	ME dipole	LTCC	5.9	0.49×0.49×0.1	26.5–40.8	45	24	Dual LP (H/V)	21	6.9 / 16.1	4×4
[8]	Diff. fed patch	PCB	3.55	0.7×0.7×0.09	26.8–29.2	8.6	N/A	Dual LP (H/V)	28 (sim.)	7.0 / 10.5	2×2
[9]	Cavity-backed patch	PCB	3.55	0.84×0.84×0.076	27.2–28.8	6	26.5	Dual LP (±45°)	28 (sim.)	7.2 / 16.7	2×8
[18]	Cavity-backed patch	PCB	2.2	0.66×0.47×0.076	37.5–52	32	N/A	Single LP	10	8.2 / -	N/A
[22]	E-shaped patch	PCB	2.2	0.46×0.7×0.076	29–46	45.4	N/A	Single LP	16	8.5 / -	N/A
[24]	Stacked patch	PCB	3.0	0.5×0.5×0.178	26–32.7	22.8	20	Dual LP (H/V)	20	6.6 / -	N/A
[28]	ME dipole	PCB	2.2	0.8×0.8×0.178	24–40	50	17.8	Dual LP (H/V)	>20	9.4 / 14.8	2×2
[32]	ME dipole	PCB	2.2	0.78×0.78×0.153	24–35	37.3	33	Dual LP (H/V)	20	9.4 / 14.85	2×2
[33]	ME dipole	FOWLP	3.85	0.61×0.61×0.119	25–43	52.9	20	Dual LP (H/V)	-	5.0 / 10.0	2×2
[38]	ME dipole	PCB	3.38	0.6×0.6×0.178	53.4–66	21.1	45 (sim.)	Dual LP (H/V)	23	8.4 / 12.5	2×2
This work	Slotted patch	PCB	3.35	0.57×0.57×0.154	23.9–43.1	57.1	36	Dual LP (±45°)	26	8.4 / 13.4	2×2

$^{(a)}$Matching criterion: –10 dB $^{(b)}$Unit cell / Array

than that of adjacent elements because of a larger physical separation.

The simulated and measured radiation patterns for the 2 × 2 array, as shown in Fig. 19, are in good agreement with a slight offset in the main beam direction. Note that the array patterns in xz and yz planes are shown at diagonal planes (D-planes) instead of E- and H-planes of the single element shown in Fig. 12. Usually, cross-polar components in the D-plane are higher than those in E- and H-planes, thereby reducing the XPD in the D-plane [60]. The simulated and measured gains are presented in Fig. 13. While the simulated array gain ranges from 8.7 to 13.9 dBi, it ranges from 7.1 to 13.4 dBi for the measured values. It can be seen that the single-element gain enhancement by using an array is lower at LB (from 24 to 26 GHz) than at UB. This is probably caused by stronger mutual coupling at LB (see Fig. 17), which leads to more power coupling to other elements (both dummy and active elements) and, hence, larger LB radiation loss [61], as well as higher cross-polarized components at LB than that at UB. The slight tilt, gain variation, and an increase in the cross-polarized component level in the measured radiation patterns compared with the simulated ones can be attributed to prototype misalignment, phase, and amplitude imbalance of differential feeding cables due to bending and fabrication tolerances. The measured sidelobe level at both planes is below −12 dB across the whole band of interest.

The performance of the proposed antenna is compared with the state of the art in Table II. It is clear that the proposed complementary antenna has a much wider impedance bandwidth than the majority of the designs in other reported works. At the same time, it remains compact in size while also having higher port-to-port isolation and a higher XPD.

V. Conclusion

A wideband differentially fed dual-polarized ME dipole for 5G mm-Wave Ka-band applications is presented. Making use of CMA, the E dipole modes and the M dipole mode are investigated individually, indicating insights into the operation of the proposed ME dipole antenna. CMA can also offer information on potential modes (e.g., J_4/J_5) in addition to the significant ones. Also, the CMA provides a better numerical knowledge of how efficiently these desired modes are excited by the differential probe feeds and of the contribution from individual electric and magnetic modes to total radiated power. It proves that the proposed ME dipole has two E dipole modes and one M dipole mode operating simultaneously, and the magnitudes of power radiated by the E and M dipoles are comparable. This is in favor of complementary antenna operation. As a result, by combining two E dipole modes (quasi-TM_{12} and quasi-TM_{31} modes) constructed by the ring patch and one M dipole mode formed by an aperture in the ring patch, the proposed antenna covers 57.1% of impedance bandwidth with stable radiation properties and port-to-port isolation greater than 36 dB across the whole operating band. The measured gains of the single element and 2×2 array are up to 8.4 and 13.4 dBi, respectively.

The proposed antenna is characterized by a planar structure with simple feeding probes that can be easily manufactured with low-cost PCB technology. Both simulations and experimental results reveal that the proposed differentially fed antenna exhibits merits of wide bandwidth, stable radiation characteristics, symmetric E- and H-plane radiation patterns over a wide bandwidth, high differential port-to-port isolation, and high XPD. Moreover, its high integration possibility and capability of surface-wave suppression imply its potential applications for 5G wireless communications and mm-Wave AiP solutions.

Acknowledgment

The authors would like to thank Prof. Ping Jack Soh for providing access to the FEKO simulation software, Aspocomp Group for PCB manufacturing, and Markku Jokinen for help in the radiation pattern measurements.

References

[1] T. Rappaport, Y. Xing, G. R. MacCartney, A. F. Molisch, E. Mellios, and J. Zhang, "Overview of millimeter wave communications for fifth-generation (5G) wireless networks-with a focus on propagation models," *IEEE Trans. Antennas Propag.*, vol. 65, no. 12, pp. 6213–6230, Dec. 2017.

[2] T. S. Rappaport *et al.*, "Millimeter wave mobile communications for 5G cellular: It will work!" *IEEE Access*, vol. 1, pp. 335–349, 2013.

[3] Y. Li, C. Wang, and Y. X. Guo, "A Ka-band wideband dual-polarized magnetoelectric dipole antenna array on LTCC," *IEEE Trans. Antennas Propag.*, vol. 68, no. 6, pp. 4985–4990, Jun. 2020.

[4] T. Tuovinen, N. Tervo, and A. Pärssinen, "Analyzing 5G RF system performance and relation to link budget for directive MIMO," *IEEE Trans. Antennas Propag.*, vol. 65, no. 12, pp. 6636–6645, Dec. 2017.

[5] Y. Zhang and J. Mao, "An overview of the development of antenna-in-package technology for highly integrated wireless devices," *Proc. IEEE*, vol. 107, no. 11, pp. 2265–2280, Nov. 2019.

[6] Q. Xue, S. W. Liao, and J. H. Xu, "A differentially-driven dual-polarized magneto-electric dipole antenna," *IEEE Trans. Antennas Propag.*, vol. 61, no. 1, pp. 425–430, Jan. 2013.

[7] R. Lian, Z. Wang, Y. Yin, J. Wu, and X. Song, "Design of a low-profile dual-polarized stepped slot antenna array for base station," *IEEE Antennas Wireless Propag. Lett.*, vol. 15, pp. 362–365, 2016.

[8] Q. Yang *et al.*, "Millimeter-wave dual-polarized differentially fed 2-D multibeam patch antenna array," *IEEE Trans. Antennas Propag.*, vol. 68, no. 10, pp. 7007–7016, Oct. 2020.

[9] Q. Yang *et al.*, "Cavity-backed slot-coupled patch antenna array with dual slant polarization for millimeter-wave base station applications," *IEEE Trans. Antennas Propag.*, vol. 69, no. 3, pp. 1404–1413, Mar. 2021.

[10] T. Hong, Z. Zhao, W. Jiang, S. Xia, Y. Liu, and S. Gong, "Dual-band SIW cavity-backed slot array using TM_{020} and TM_{120} modes for 5G applications," *IEEE Trans. Antennas Propag.*, vol. 67, no. 5, pp. 3490–3495, May 2019.

[11] T. Deckmyn, M. Cauwe, D. V. Ginste, H. Rogier, and S. Agneessens, "Dual-band (28,38) GHz coupled quarter-mode substrate-integrated waveguide antenna array for next-generation wireless systems," *IEEE Trans. Antennas Propag.*, vol. 67, no. 4, pp. 2405–2412, Apr. 2019.

[12] Y.-X. Sun, D. Wu, X. S. Fang, and N. Yang, "Compact quarter-mode substrate-integrated waveguide dual-frequency millimeter-wave antenna array for 5G applications," *IEEE Antennas Wireless Propag. Lett.*, vol. 19, no. 8, pp. 1405–1409, Aug. 2020.

[13] G. Xu *et al.*, "Microstrip grid and patch-based dual-band shared-aperture differentially fed array antenna," *IEEE Antennas Wireless Propag. Lett.*, vol. 20, no. 6, pp. 1043–1047, Jun. 2021.

[14] M. Ferrando-Rocher, J. I. Herranz-Herruzo, A. Valero-Nogueira, and B. Bernardo-Clemente, "Full-metal K-Ka dual-band shared-aperture array antenna fed by combined ridge-groove gap waveguide," *IEEE Antennas Wireless Propag. Lett.*, vol. 18, no. 7, pp. 1463–1467, Jul. 2019.

[15] Y.-X. Sun and K. W. Leung, "Substrate-integrated two-port dual-frequency antenna," *IEEE Trans. Antennas Propag.*, vol. 64, no. 8, pp. 3692–3697, Aug. 2016.

[16] J. F. Zhang, Y. J. Cheng, Y. R. Ding, and C. X. Bai, "A dual-band shared-aperture antenna with large frequency ratio, high aperture reuse efficiency, and high channel isolation," *IEEE Trans. Antennas Propag.*, vol. 67, no. 2, pp. 853–860, Feb. 2019.

[17] G. Xu, H.-L. Peng, Z. Shao, L. Zhou, Y. Zhang, and W.-Y. Yin, "Dual-band differential shifted-feed microstrip grid array antenna with two parasitic patches," *IEEE Trans. Antennas Propag.*, vol. 68, no. 3, pp. 2434–2439, Mar. 2020.

[18] K. Fan, Z.-C. Hao, and Q. Yuan, "A low-profile wideband substrate-integrated waveguide cavity-backed E-shaped patch antenna for the Q-LINKPAN applications," *IEEE Trans. Antennas Propag.*, vol. 65, no. 11, pp. 5667–5676, Nov. 2017.

[19] H. Li, Y. Li, L. Chang, W. Sun, X. Qin, and H. Wang, "A wideband dual-polarized endfire antenna array with overlapped apertures and small clearance for 5G millimeter-wave applications," *IEEE Trans. Antennas Propag.*, vol. 69, no. 2, pp. 815–824, Feb. 2021.

[20] T. Li and Z. N. Chen, "Wideband sidelobe-level reduced Ka-band metasurface antenna array fed by substrate-integrated gap waveguide using characteristic mode analysis," *IEEE Trans. Antennas Propag.*, vol. 68, no. 3, pp. 1356–1365, Mar. 2020.

[21] K. Zhang, Z. H. Jiang, W. Hong, and D. H. Werner, "A low-profile and wideband triple-mode antenna for wireless body area network concurrent on-/off-body communications," *IEEE Trans. Antennas Propag.*, vol. 68, no. 3, pp. 1982–1994, Mar. 2020.

[22] J. Yin, Q. Wu, C. Yu, H. Wang, and W. Hong, "Broadband symmetrical E-shaped patch antenna with multimode resonance for 5G millimeter-wave applications," *IEEE Trans. Antennas Propag.*, vol. 67, no. 7, pp. 4474–4483, Jul. 2019.

[23] P. A. Dzagbletey and Y. B. Jung, "Stacked microstrip linear array for millimeter-wave 5G baseband communication," *IEEE Antennas Wireless Propag. Lett.*, vol. 17, no. 5, pp. 780–783, May 2018.

[24] T. Chaloun, V. Ziegler, and W. Menzel, "Design of a dual-polarized stacked patch antenna for wide-angle scanning reflectarrays," *IEEE Trans. Antennas Propag.*, vol. 64, no. 8, pp. 3380–3390, Aug. 2016.

[25] K.-M. Luk and H. Wong, "A new wideband unidirectional antenna element," *Int. J. Microw. Opt. Technol.*, vol. 1, no. 1, pp. 35–44, Jul. 2006.

[26] K.-M. Luk and B. Wu, "The magnetoelectric dipole—A wideband antenna for base stations in mobile communications," *Proc. IEEE*, vol. 100, no. 7, pp. 2297–2307, Jul. 2012.

[27] M. Li and K.-M. Luk, "Wideband magneto-electric dipole antenna for 60-GHz millimeter-wave communications," *IEEE Trans. Antennas Propag.*, vol. 63, no. 7, pp. 3276–3279, Jul. 2015.

[28] X. Dai and K. M. Luk, "A wideband dual-polarized antenna for millimeter-wave applications," *IEEE Trans. Antennas Propag.*, vol. 69, no. 4, pp. 2380–2385, Apr. 2021.

[29] D. Shen, C. Ma, W. Ren, X. Zhang, Z. Ma, and R. Qian, "A low-profile substrate-integrated-gap-waveguide-fed magnetoelectric dipole," *IEEE Antennas Wireless Propag. Lett.*, vol. 17, no. 8, pp. 1373–1376, Aug. 2018.

[30] A. Dadgarpour, N. Bayat-Makou, M. A. Antoniades, A. A. Kishk, and A. Sebak, "A dual-polarized magnetoelectric dipole array based on printed ridge gap waveguide with dual-polarized split-ring resonator lens," *IEEE Trans. Antennas Propag.*, vol. 68, no. 5, pp. 3578–3585, May 2020.

[31] F. Wu, J. Wang, R. Lu, X. Xia, W. Hong, and K.-M. Luk, "Wideband and low cross-polarization transmitarray using 1 bit magnetoelectric dipole elements," *IEEE Trans. Antennas Propag.*, vol. 69, no. 5, pp. 2605–2614, May 2021.

[32] Y. Cheng and Y. Dong, "Dual-broadband dual-polarized shared-aperture magnetoelectric dipole antenna for 5G applications," *IEEE Trans. Antennas Propag.*, vol. 69, no. 11, pp. 7918–7923, Nov. 2021.

[33] B. Yu *et al.*, "A wideband mmWave antenna in fan-out wafer level packaging with tall vertical interconnects for 5G wireless communication," *IEEE Trans. Antennas Propag.*, vol. 69, no. 10, pp. 6906–6911, Oct. 2021.

[34] Y. Fang and Y. P. Zhang, "On surface-wave suppression of differential circular microstrip antennas," *IEEE Antennas Wireless Propag. Lett.*, vol. 20, no. 9, pp. 1691–1695, Sep. 2021.

[35] Z. Shao, L.-F. Qiu, and Y. P. Zhang, "Design of wideband differentially fed multilayer stacked patch antennas based on bat algorithm," *IEEE Antennas Wireless Propag. Lett.*, vol. 19, no. 7, pp. 1172–1176, Jul. 2020.

[36] R. Garg, P. Bhartia, I. Bahl, and A. Ittipiboon, *Microstrip Antenna Design Handbook*. Norwood, MA, USA: Artech House, 2001.

[37] R. E. Amaya, M. Li, K. Hettak, and C. J. Verver, "A broadband 3D vertical microstrip to stripline transition in LTCC using a quasi-coaxial structure for millimetre-wave SOP applications," in *Proc. Eur. Microw. Conf.*, Paris, France, Sep. 2010, pp. 109–112.

[38] Y. Li and K.-M. Luk, "60-GHz dual-polarized two-dimensional switch-beam wideband antenna array of aperture-coupled magneto-electric dipoles," *IEEE Trans. Antennas Propag.*, vol. 64, no. 2, pp. 554–563, Feb. 2016.

[39] X. Gu *et al.*, "Development, implementation, and characterization of a 64-element dual-polarized phased-array antenna module for 28-GHz high-speed data communications," *IEEE Trans. Microw. Theory Techn.*, vol. 67, no. 7, pp. 2975–2984, Jul. 2019.

[40] R. F. Harrington and J. R. Mautz, "Theory of characteristic modes for conducting bodies," *IEEE Trans. Antennas Propag.*, vol. AP-19, no. 5, pp. 622–628, May 1971.

[41] M. Khan and M. Chowdhury, "Analysis of modal excitation in wideband slot-loaded microstrip patch antenna using theory of characteristic modes," *IEEE Trans. Antennas Propag.*, vol. 68, no. 11, pp. 7618–7623, Nov. 2020.

[42] F. H. Lin and Z. N. Chen, "Low-profile wideband metasurface antennas using characteristic mode analysis," *IEEE Trans. Antennas Propag.*, vol. 65, no. 4, pp. 1706–1713, Apr. 2017.

[43] F. H. Lin and Z. N. Chen, "Resonant metasurface antennas with resonant apertures: Characteristic mode analysis and dual-polarized broadband low-profile design," *IEEE Trans. Antennas Propag.*, vol. 69, no. 6, pp. 3512–3516, Jun. 2021.

[44] J.-F. Lin and Q.-X. Chu, "Increasing bandwidth of slot antennas with combined characteristic modes," *IEEE Trans. Antennas Propag.*, vol. 66, no. 6, pp. 3148–3153, Jun. 2018.

[45] Y. Chen and C.-F. Wang, *Characteristic Modes: Theory and Applications in Antenna Engineering*. Hoboken, NJ, USA: Wiley, 2015.

[46] E. Safin and D. Manteuffel, "Reconstruction of the characteristic modes on an antenna based on the radiated far field," *IEEE Trans. Antennas Propag.*, vol. 61, no. 6, pp. 2964–2971, Jun. 2013.

[47] J. J. Borchardt and T. C. Lapointe, "U-slot patch antenna principle and design methodology using characteristic mode analysis and coupled mode theory," *IEEE Access*, vol. 7, pp. 109375–109385, 2019.

[48] A. Das, S. P. Mathur, and S. K. Das, "Radiation characteristics of higher-order modes in microstrip ring antenna," *IEE Proc. H-Microw., Opt. Antennas*, vol. 131, no. 2, pp. 102–106, Apr. 1984.

[49] D. K. Cheng, *Field and Wave Electromagnetics*. Reading, MA, USA: Addison-Wesley, 1989.

[50] L. Shen, S. A. Long, M. Allerding, and M. Walton, "Resonant frequency of a circular disc, printed-circuit antenna," *IEEE Trans. Antennas Propag.*, vol. AP-25, no. 4, pp. 595–596, Jul. 1977.

[51] N. M. Mohamed-Hicho, E. Antonino-Daviu, M. Cabedo-Fabrés, and M. Ferrando-Bataller, "Designing slot antennas in finite platforms using characteristic modes," *IEEE Access*, vol. 6, pp. 41346–41355, 2018.

[52] E. Antonino-Daviu, M. Cabedo-Fabrés, M. Sonkki, N. M. Mohamed-Hicho, and M. Ferrando-Bataller, "Design guidelines for the excitation of characteristic modes in slotted planar structures," *IEEE Trans. Antennas Propag.*, vol. 64, no. 12, pp. 5020–5029, Dec. 2016.

[53] N.-W. Liu, L. Zhu, W.-W. Choi, and J.-D. Zhang, "A novel differential-fed patch antenna on stepped-impedance resonator with enhanced bandwidth under dual-resonance," *IEEE Trans. Antennas Propag.*, vol. 64, no. 11, pp. 4618–4625, Nov. 2016.

[54] D. Pozar, *Microwave Engineering*, 4th ed. Hoboken, NJ, USA: Wiley, 2011.

[55] G. F. Engen and C. A. Hoer, "Thru-reflect-line: An improved technique for calibrating the dual six-port automatic network analyzer," *IEEE Trans. Microw. Theory Techn.*, vol. MTT-27, no. 12, pp. 987–993, Dec. 1979.

[56] L. Sun, Y. Li, Z. Zhang, and H. Wang, "Antenna decoupling by common and differential modes cancellation," *IEEE Trans. Antennas Propag.*, vol. 69, no. 2, pp. 672–682, Feb. 2021.

[57] N. Tervo *et al.*, "Combined sidelobe reduction and omnidirectional linearization of phased array by using tapered power amplifier biasing and digital predistortion," *IEEE Trans. Microw. Theory Techn.*, vol. 69, no. 9, pp. 4284–4299, Sep. 2021.

[58] F. Wu and K.-M. Luk, "A reconfigurable magneto-electric dipole antenna using bent cross-dipole feed for polarization diversity," *IEEE Antennas Wireless Propag. Lett.*, vol. 16, pp. 412–415, 2017.

[59] K. A. Obeidat, B. D. Raines, and R. G. Rojas, "Discussion of series and parallel resonance phenomena in the input impedance of antennas," *Radio Sci.*, vol. 45, no. 6, pp. 1–9, Dec. 2010.

[60] N. A. Aboserwal, J. L. Salazar, J. A. Ortiz, J. D. Díaz, C. Fulton, and R. D. Palmer, "Source current polarization impact on the cross-polarization definition of practical antenna elements: Theory and applications," *IEEE Trans. Antennas Propag.*, vol. 66, no. 9, pp. 4391–4406, Sep. 2018.

[61] K. Rasilainen, A. Lehtovuori, and V. Viikari, "LTE handset antenna with closely-located radiators, low-band MIMO, and high efficiency," in *Proc. 11th Eur. Conf. Antennas Propag. (EUCAP)*, Paris, France, Mar. 2017, pp. 3074–3078.

Jiangcheng Chen (Graduate Student Member, IEEE) received the B.Sc. degree in communication engineering from Fuzhou University, Fuzhou, China, in 2012, and the M.Sc. degree in communication engineering from The University of Manchester, Manchester, U.K., in 2013. He is currently pursuing the Ph.D. degree in communication engineering with the Centre for Wireless Communications, University of Oulu, Oulu, Finland.

He joined the Centre for Wireless Communications, University of Oulu, as a Researcher, in 2016. He holds one U.S. patent. His current research interests include wearable antennas, millimeter-wave (mm-Wave) antennas, metasurfaces, and THz on-chip antennas.

Markus Berg received the M.Sc. (Tech.) and D.Sc. degrees in electrical engineering from the University of Oulu, Oulu, Finland, in 2005 and 2011, respectively.

From 2005 to 2017, he was a Research Scientist and a Project Manager with the Centre for Wireless Communications, University of Oulu. In 2015, he was a Design Engineer with Elektrobit, Oulu, and Bittium Corporation, Oulu. Since 2017, he has been a Senior Research Fellow and an Adjunct Professor with the Faculty of Information Technology and Electrical Engineering, University of Oulu. In 2018, he founded ExcellAnt Ltd., Oulu, where he is currently a Senior Antenna Advisor. He has authored or coauthored more than 90 international journal articles and conference papers. He holds one U.S. patent. His current research interests include antennas and propagation for wireless communication, sub-THz integrated antennas, and global navigation satellite systems (GNSS) reflectometry.

Kimmo Rasilainen (Member, IEEE) was born in Helsinki, Finland, in 1987. He received the B.Sc. (Tech.), M.Sc. (Tech.) (Hons.), and D.Sc. (Tech.) degrees in electrical engineering from the School of Electrical Engineering, Aalto University, Espoo, Finland, in 2012, 2013, and 2017, respectively.

From 2009 to 2017, he was with the Department of Electronics and Nanoengineering, School of Electrical Engineering, Aalto University, first as a Research Assistant and later as a Research Scientist, working on handset antennas and wireless sensors. From 2017 to 2020, he was a Post-Doctoral Researcher with the Department of Microtechnology and Nanoscience, Chalmers University of Technology, Gothenburg, Sweden, working on the integration of millimeter-wave (mm-Wave) communications' assemblies and thermal simulations. Since 2020, he has been a Post-Doctoral Researcher with the Centre for Wireless Communications, University of Oulu, Oulu, Finland. He has authored or coauthored more than 35 international journal articles and conference papers. His current research interests include mm-wave and THz antennas, microwave engineering, material characterization, and thermal analysis.

Zeeshan Siddiqui (Graduate Student Member, IEEE) received the B.S. degree in electronic engineering from the Sir Syed University of Engineering and Technology, Karachi, Pakistan, in 2003, and the M.Sc. degree in wireless networks from the Queen Mary College, University of London, London, U.K., in 2006. He is currently pursuing the Ph.D. degree in communications engineering with the Centre for Wireless Communications, University of Oulu, Oulu, Finland.

He was a Researcher with the Prince Sultan Advanced Technology Research Institute, King Saud University, Riyadh, Saudi Arabia, from 2009 to 2016. His current research interests include leaky wave antennas, wideband and multiband antennas, and phased arrays.

Marko E. Leinonen (Member, IEEE) received the M.Sc., Licentiate in Technology, and Dr.Sc. degrees in electrical engineering from the University of Oulu, Oulu, Finland, in 1996, 2002, and 2020, respectively.

From 1994 to 2012, he was with Nokia Mobile Phones, Oulu, working in various positions with radio engineering and technology management. From 2006 to 2007, he was a senior engineering manager in Bengaluru, India. From 2012 to 2016, he was a Master Developer with Ericsson, Oulu. Since 2017, he has been with the Centre for Wireless Communications, University of Oulu, where he is currently a Research Director. He holds over 40 granted international patent families concentrating on radio engineering. His research interests include wireless radio systems and quality topics in radio engineering.

Aarno Pärssinen (Senior Member, IEEE) received the M.Sc., Licentiate in Technology, and D.Sc. degrees in electrical engineering from the Helsinki University of Technology, Espoo, Finland, in 1995, 1997, and 2000, respectively.

From 1994 to 2000, he was with the Electronic Circuit Design Laboratory, Helsinki University of Technology, working on direct conversion receivers and subsampling mixers for wireless communications. In 1996, he was a Research Visitor with the University of California at Santa Barbara, Santa Barbara, CA, USA. From 2000 to 2011, he was with the Nokia Research Center, Helsinki, Finland. From 2009 to 2011, he was a member of the Nokia CEO Technology Council, Helsinki. From 2011 to 2013, he was with Renesas Mobile Corporation, Helsinki, working as a Distinguished Researcher and an RF Research Manager. From October 2013 to September 2014, he was an Associate Technical Director with Broadcom, Helsinki. Since September 2014, he has been with the Centre for Wireless Communications, University of Oulu, Oulu, Finland, where he is currently a Professor. He leads the devices and circuits research area in the 6G Flagship Program financed by the Academy of Finland, Helsinki. He is also one of the original contributors to Bluetooth low-energy extension, now called BT LE. He has authored and coauthored one book, two book chapters, and more than 180 international journal articles and conference papers. He holds several patents. His research interests include wireless systems and transceiver architectures for wireless communications with special emphasis on RF and analog integrated circuit and system design.

Dr. Pärssinen has served as a member of the Technical Program Committee of the International Solid-State Circuits Conference from 2007 to 2017, where he was the Chair of the European Regional Committee from 2012 to 2013 and the Wireless Sub-Committee from 2014 to 2017. He was a recipient of the European Microwave Price on the Best Paper of the European Microwave Conference 2020. He has served as a Solid-State Circuits Society Representative for the IEEE 5G Initiative from 2015 to 2019.